Materials Advances

ROYAL SOCIETY OF CHEMISTRY

PAPER

View Article Online
View Journal

Cite this: DOI: 10.1039/d6ma00351f

Phosphorus-doped carbon quantum dots for broadband self-powered n-Si Schottky photodetectors with enhanced quantum efficiency and detectivity

Ali Akbar Hussaini, [a] Mütahire Tok,[bc] Kurtuluş Yılmaz, [b] Çisem Kırbıyık Kurukavak, *[b] Mahmut Kuş, [b] Beyza Terzi [a] and Murat Yıldırım [a]

The interfacial energetics of metal–semiconductor junctions critically determine the carrier transport behavior and overall performance of Schottky-based optoelectronic devices. In this work, unmodified carbon quantum dots (CQDs) and phosphorus-doped carbon quantum dots (P-CQDs) were synthesized and comprehensively characterized through transmission electron microscopy (TEM), photoluminescence (PL) spectroscopy, Fourier-transform infrared (FTIR) spectroscopy, UV-Vis spectroscopy (UV-Vis), and scanning electron microscopy coupled with energy-dispersive X-ray spectroscopy (SEM–EDS). The engineered quantum dots were subsequently integrated into n-Si heterojunction architectures to investigate the influence of heteroatom-induced band structure modulation on broadband self-powered photodetection. Under zero-bias operation, the P-CQD/n-Si photodetector demonstrated markedly enhanced optoelectronic performance compared to the undoped CQD/n-Si device. The photocurrent increased from 2.22 × 10^{-5} A (CQD/n-Si) to 9.66 × 10^{-5} A (P-CQD/n-Si) under 100 mW cm^{-2} illumination. The maximum responsivity reached 0.386 A W^{-1}, while specific detectivity achieved 6.99 × 10^{10} Jones, accompanied by a low noise-equivalent power of 1.46 × 10^{-12} W $Hz^{-1/2}$. Broadband spectral sensitivity spanning 351–1600 nm was achieved, with pronounced enhancement in the visible–NIR region. Notably, the external quantum efficiency (EQE) was significantly enhanced from ∼3.34% in the undoped device to ∼22.88% after phosphorus doping, corresponding to an approximately sevenfold improvement in photon-to-charge conversion efficiency. Overall, phosphorus doping provides an effective strategy for tailoring interfacial barrier properties and quantum dot electronic structure, enabling high-responsivity, low-noise, and high-efficiency self-powered photodetectors suitable for next-generation wide-band optoelectronic applications.

Received 12th March 2026,
Accepted 28th April 2026

DOI: 10.1039/d6ma00351f

rsc.li/materials-advances

1. Introduction

The fundamental operating principles and performance parameters of modern electronic and optoelectronic devices are determined by the potential barrier profiles formed at metal-semiconductor interfaces and their significant effects on carrier transport mechanisms.[1] Schottky contact energy barriers are shaped by interface dipole rearrangements, Fermi level pinning, thermionic emission, and the impact of local defect distributions. As a result, these variables influence the device's electrical properties.[2,3] Schottky diodes are strategically significant not only in classical electronic circuits but also in broadband photodetection, high-speed optical switching, integrated photonic platforms, and sensor technologies due to their low forward-bias threshold voltage, fast switching capability, and stable operating performance at high frequencies.[4–10] In particular, in broad-spectrum photodetector applications extending to the UV-vis-NIR regions, diode architectures optimized through interface engineering offer significant advantages in terms of optimizing photon absorption processes, exciton separation, and carrier collection efficiency.[11–14] Integrating functional nanostructures into the active layer is one of the most effective ways to improve the performance of diodes and photodetectors, as the existing literature has shown. Charge carrier

[a] Department of Biotechnology, Faculty of Science, Selcuk University, Konya, Turkey. E-mail: aliakbar.hussaini.1994@gmail.com, beyzaterzi18@gmail.com, muratyildirim@selcuk.edu.tr
[b] Department of Chemical Engineering, Konya Technical University, 42075, Konya, Turkey. E-mail: ckirbiyik@ktun.edu.tr, mutahiretok@yiu.edu.tr, kurtulusyilmaz3@gmail.com, mahmutkus1@gmail.com
[c] Department of Pharmacy Services, Vocational School, Yuksek Ihtisas University, 06291 Ankara, Turkey

dynamics can be modulated and interface energy levels can be realigned through this integration.[15,16] In this context, carbon quantum dots (CQDs) have become an extremely attractive material class for next-generation optoelectronic systems due to their pronounced quantum confinement effect, high surface-to-volume ratio, chemical stability, low toxicity, and rich surface functionalization possibilities.[17–22] However, the electronic band structures of pure CQDs are unable to fully achieve the targeted optoelectronic efficiency in most cases due to surface-induced trap states, insufficient passivation, high defect levels, and limited absorption intensity.[23–26] Therefore, heteroatom doping can be regarded a strategic approach that enables the atomic-level redesign of fundamental optoelectronic properties, including modulation of the bandgap, redistribution of electron density, dipole formation at the surface level, and minimization of defect energy, in quantum dots.[27–29] The integration of heteroatoms, such as nitrogen, sulphur, phosphorus and boron, into the carbon skeleton can be achieved by rearranging the charge density distribution. This process enables the modulation of the band gap, extends the carrier lifetime by passivating surface defects, and significantly increases light absorption capacity across broad spectral regions.[30,31] Phosphorus doping is a significant dopant type in optoelectronic devices. This consideration is primarily due to the high electron donor capacity inherent in the dopant, and to its capacity to contribute to the passivation of surface defects by means of C–O–P and C–P bonding configurations. Furthermore, phosphorus doping is able to enhance the broad-band absorption regime.[31]

Despite the extensive research that has been conducted on the use of heteroatom doping as a method for adjusting the optoelectronic characteristics of CQDs, the underlying mechanisms that govern the interaction of these structures with device interfaces and their impact on optoelectronic device performance remain to be fully elucidated. While it has been reported that phosphorus doping affects the electronic structure of CQDs, the clear correlation between phosphorus-induced surface state modulation, defect passivation behavior, and charge carrier dynamics at the interface has not yet been clearly established. In this context, the present study adopts a novel approach by exploring a comprehensive structure–property–performance relationship that extends beyond traditional doping methods. Phosphorus-doped CQDs have been utilized as a functional interface regulator to organize energy level alignment and suppress interface-induced trap-assisted recombination. This dual effect enables more efficient charge extraction within the device and reduced non-radiative losses. Moreover, while earlier studies have predominantly concentrated on enhancements at the material level, this study demonstrates a performance enhancement at the device level supported by mechanistic insights and highlights the critical role of phosphor-induced electronic modulation in the optimization of interfacial processes. These findings have two principal implications. Firstly, they result in an increase in the efficiency of the device. Secondly, they provide a deeper understanding of how CQDs designed through heteroatom engineering can be rationally developed for advanced optoelectronic applications.

In the present study, unmodified carbon quantum dots (CQD) and phosphorus-doped carbon quantum dots (P-CQD) have been synthesized. A range of characterization techniques were then employed to examine the optical, structural and electronic properties of the synthesized nanomaterials in detail. UV-vis spectroscopy and photoluminescence measurements were utilized to evaluate band transitions, defect-induced emission processes, and the quantum confinement effect. The application of TEM provided high-resolution information on the size, morphology, and crystallinity of the synthesized particles. SEM coupled with EDX was used to examine the surface morphology, elemental composition, and confirm the presence of dopants. FTIR analysis was employed to identify surface functional groups and heteroatom bonding. Additionally, UV-vis spectroscopy was used to investigate the optical properties and determine the bandgap of the quantum dots. The results obtained demonstrate that P-doped CQD not only enhance optical performance through strong photon absorption properties across broad spectral regions but also improve carrier transport and injection efficiency by enhancing energy level alignment at metal–semiconductor interfaces. In this context, the study provides original and significant contributions towards the feasibility of utilizing heteroatom-engineered carbon-based quantum dots as high-performance functional components in next-generation photodetectors, Schottky diodes, and wide-band optoelectronic device architectures.

2. Experimental details

2.1. Reagents

Citric acid (≥99%, Sigma-Aldrich) and orthophosphoric acid (85%, Merck) were used as precursors without further purification. Ultrapure water (18.2 MΩ cm) was employed throughout the experiments. Dimethylformamide (DMF, analytical grade) was used as a solvent for optical characterization.

2.2. Synthesis of CQDs and P-CQD

The synthesis of unmodified carbon quantum dots (CQD) was carried out using a hydrothermal method. For this purpose, 1.5 g of citric acid (99% purity; Sigma-Aldrich) was homogenized in 100 mL of distilled water at room temperature for 20 minutes using a magnetic stirrer. The resulting solution was transferred to a Teflon-lined stainless-steel autoclave and subjected to hydrothermal treatment at 180 °C for 18 hours. Following the conclusion of the reaction time, a dark brown solution was obtained, which is an indication of CQD formation. The product was isolated from the solvent phase by means of centrifugation at 6000 rpm for a period of 30 minutes, after which it was washed with ultrapure water. The washing process was repeated on three occasions, with each step being followed by centrifugation. The solid product obtained was dried in an oven at 80 °C for 24 hours and stored in a refrigerator with the objective of conducting further studies in relation to its characterization and application.

The synthesis of phosphorus-doped carbon quantum dots (P-CQDs) was carried out using the solvothermal method. In the initial step of the procedure, 1.5 g of citric acid (99% pure, obtained from Sigma-Aldrich) was combined with 5 mL of concentrated H_3PO_4 solution (also 99% pure, obtained from Sigma-Aldrich) and 100 mL of *N*,*N*-dimethylformamide (DMF). The mixture was then stirred at room temperature for a period of 20 minutes, until a homogeneous solution was achieved. The prepared solution was transferred to a Teflon-lined stainless-steel autoclave and subjected to solvothermal treatment at 180 °C for 24 hours. Following the conclusion of the reaction, a dark brown solution was obtained, which is indicative of P-CQD formation. The product was isolated from the solvent through a process of centrifugation at 6000 rpm for a duration of 30 minutes, after which it was thoroughly washed with ultrapure water. The washing process was repeated on three occasions. The product was subjected to a drying process in an oven at a temperature of 80 °C for a duration of 24 hours. After this, it was stored within a refrigerator, with the objective of conducting further studies in relation to its characterizations and application.

2.3. Device fabrication

Initially, an aluminum (Al) ohmic back contact with a thickness of 120 nm was deposited onto the rear surface of the n-type silicon (n-Si) substrate using the physical vapor deposition (PVD) technique. Following deposition, the samples were thermally annealed at 400 °C for 5 minutes to improve metal–semiconductor contact quality and ensure stable Ohmic behavior. Subsequently, CQD and P-CQD solutions were prepared at a concentration of 7.5 mg mL^{-1} in distilled water. The prepared solutions were spin-coated onto the polished front surface of the n-Si substrates at 1500 rpm for 40 seconds to form uniform thin films. After deposition, the films were heated at 60 °C to remove residual solvent and promote film stabilization. Finally, a 120 nm thick silver (Ag) layer was deposited onto the active layer *via* PVD to form the top Schottky contact, completing the device structure. This process resulted in CQD/n-Si and P-CQD/n-Si heterojunction-based photodetector structures. After the deposition of the active layer, the electrical contacts of the devices were defined and formed by means of the PVD method, whereupon the devices were made ready for testing to facilitate advanced electrical and optoelectronic characterizations. The production stages of CQD/n-Si and P-CQD/n-Si-based photodetector devices are shown schematically in Fig. 1a. The energy band diagrams of the CQD/n-Si and P-CQD/n-Si heterojunction devices, shown in Fig. 1b and c, illustrate the charge transport mechanisms and interfacial energetics governing device performance. In both structures, the CQDs form a junction with n-type silicon, creating a built-in potential that facilitates efficient charge separation. The optical bandgaps used in the band diagram were obtained from our experimental UV-vis measurements, yielding

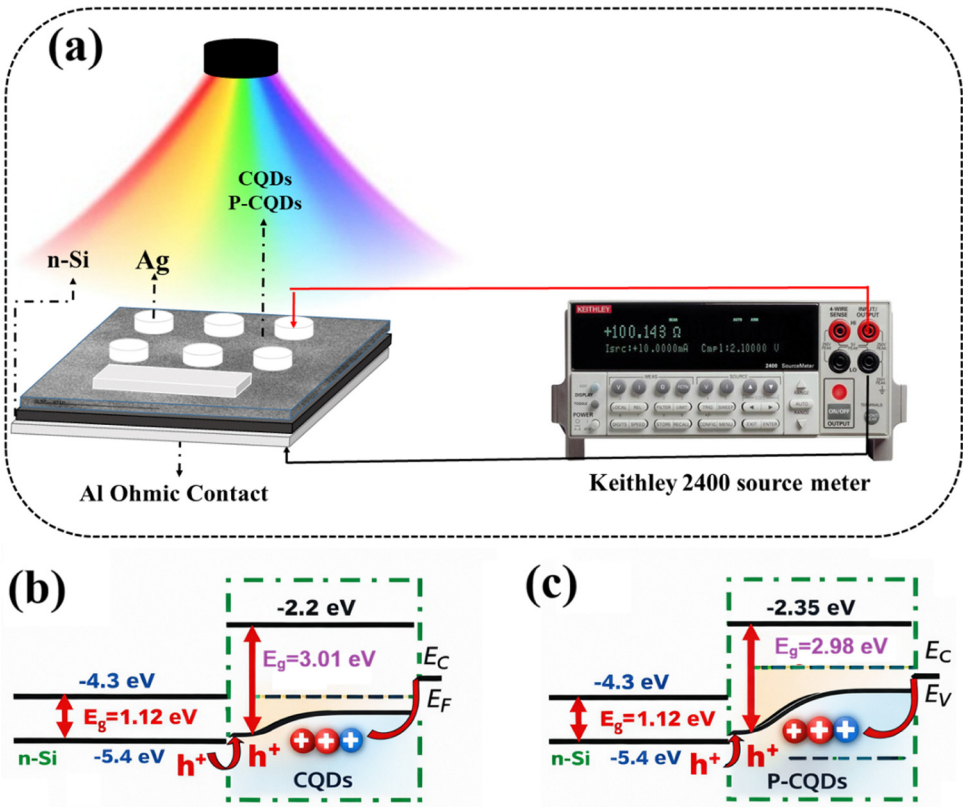

Fig. 1 (a) Schematic illustration of the CQD/n-Si and P-CQD/n-Si photodetector devices. Band diagrams of the (b) CQD/n-Si and (c) P-CQD/n-Si devices.

values of 3.01 eV for CQDs and 2.98 eV for P-CQDs. The slight reduction in bandgap upon phosphorus doping indicates a modification of the electronic structure. Assuming a similar conduction band position, this reduction results in a slight upward shift of the valence band maximum, which can enhance hole transport across the interface. Furthermore, the alignment of energy levels between the quantum dots and n-Si promotes efficient electron transfer from the CQDs to the silicon substrate, while holes are transported in the opposite direction. The improved device performance observed in the P-CQD/n-Si device can therefore be attributed to subtle changes in band alignment and reduced interfacial barriers, facilitating more efficient charge separation and transport.

3. Results and discussion

3.1. Structural, morphological, and optical characterization

The FTIR spectra shown in Fig. 2a indicate the surface functional groups of CQD synthesized using citric acid and P-CQD obtained by phosphoric acid doping. The broad absorption band observed in the CQD spectrum in the range of 3000–3600 cm^{-1} corresponds to hydroxyl (–OH) stretching vibrations, while the band at 2980 cm^{-1} corresponds to aliphatic C–H stretching vibrations. Along with this, the bands observed at 1654 cm^{-1} and 1549 cm^{-1} are attributed to C═O and C═C stretching vibrations, respectively. The bands at 1387 cm^{-1} and 1060 cm^{-1} originate from the asymmetric and symmetric stretching vibrations of the C–O–C and C–O groups,

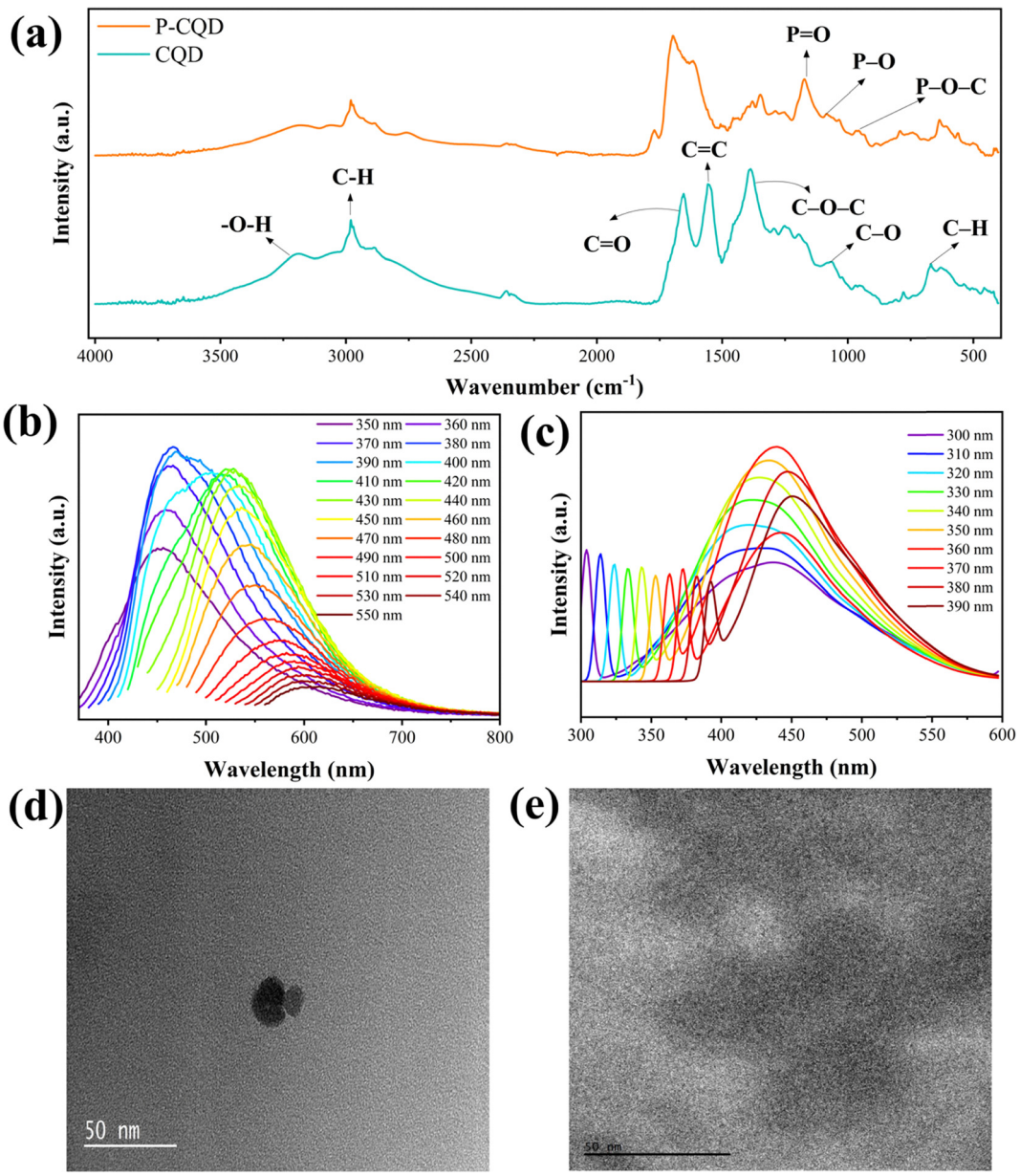

Fig. 2 (a) FTIR spectra of CQD and P-CQD. PL spectra of (b) undoped-CQD and (c) P-CQD obtained at a variety of excitation wavelengths. TEM images of (d) undoped CQDs and (e) phosphorus-doped CQDs (P-CQDs).

respectively. The weak band observed around 650 cm^{-1} is associated with aromatic C–H out-of-plane bending vibration.[32–34] The presence of these functional groups confirms that the surface of CQD synthesized using citric acid is rich in oxygen-containing functional groups. In the FTIR spectrum of P-CQDs, the –OH bands at 3000–3600 cm^{-1} and the C–H band at 2980 cm^{-1} are preserved, while additional bands observed at 956, 1076, and 1168 cm^{-1} can be attributed to the stretching vibrations of P–O–C, P–O, and P═O functional groups, respectively.[35,36] The presence of these phosphorus-related functional groups indicates that CQDs have been successfully doped with phosphorus.

The photoluminescence (PL) spectra of pure CQD samples exhibit a distinct emission behavior that is dependent on the excitation wavelength across the 350–550 nm excitation range, as shown in Fig. 2b. The observation of increasingly intense and relatively narrow emission bands at lower excitation wavelengths indicates the prevalence of radiative recombination originating from core states. Conversely, as the excitation wavelength increases, the red shift of the emission maximum and the broadening of the bandwidth reveal the increased contribution of surface states and defect-mediated transitions.[37,38] This is consistent with the heterogeneous electronic structure of CQDs, arising from their size distribution and surface functional groups. In contrast, P-CQDs exhibit a distinct PL behavior, characterized by increased emission intensity and a more stable emission profile against varying excitation energies, as shown in Fig. 2c. The suppression of spectral broadening and the decrease in excitation wavelength-dependent peak shift indicate that phosphorus doping modifies the surface electronic structure, creating a passivation effect and rearranging localized energy levels. Furthermore, the more pronounced Stokes shift observed in phosphorus-doped CQDs supports the formation of new emissive states due to doping. Consequently, phosphorus doping enhances the photophysical stability of the system by regulating the emission balance between core and surface states and conferring tunable optical properties.[35] The TEM image displayed in Fig. 2d illustrates that non-doped carbon quantum dots (CQDs) possess nanoscopic dimensions and a well-defined morphology. The diameters of the non-doped CQDs depicted are estimated to be in the order of a few nanometers, based on a rough estimation using a 50 nm scale bar, and are mostly in the range of ~4–7 nm. This size range is consistent with the values commonly reported in the literature for carbon quantum dots,[39] suggesting that the synthesized nanostructures are within the size regime where the quantum confinement effect is effective. As demonstrated in Fig. 2e, the morphological characteristics and size distributions of phosphorus-doped carbon quantum dots (P-CQDs) were examined using transmission electron microscopy (TEM). The application of transmission electron microscopy (TEM) has revealed that P-CQDs possess a well-dispersed, nano-sized structure that is largely free from agglomeration. An evaluation employing a 50 nm scale bar yielded an average diameter of approximately 3–7 nm for individual CQD particles. The TEM findings obtained in this study confirm that phosphorus doping preserves the morphology of carbon quantum dots and creates a homogeneous nanostructure.[31,40]

SEM–EDX analysis was conducted to confirm the morphological integrity of the P-CQDs and to ascertain the success of the phosphorus doping process. As illustrated in Fig. 3a, the SEM image indicates that the sample exhibits a homogeneous surface morphology at the micrometers scale, with no discernible agglomeration or phase separation. As demonstrated in Fig. 3b, the EDX spectrum unequivocally indicates the presence of carbon, oxygen, and phosphorus elements within the carbon matrix. The elemental mapping results presented in Fig. 3c–f demonstrate that these elements are distributed uniformly throughout the analysis area. In particular, the homogeneous distribution of phosphorus within the carbon matrix, without localization, indicates that the P-doping is effectively integrated into the structure. The findings indicate that P-CQDs possess a

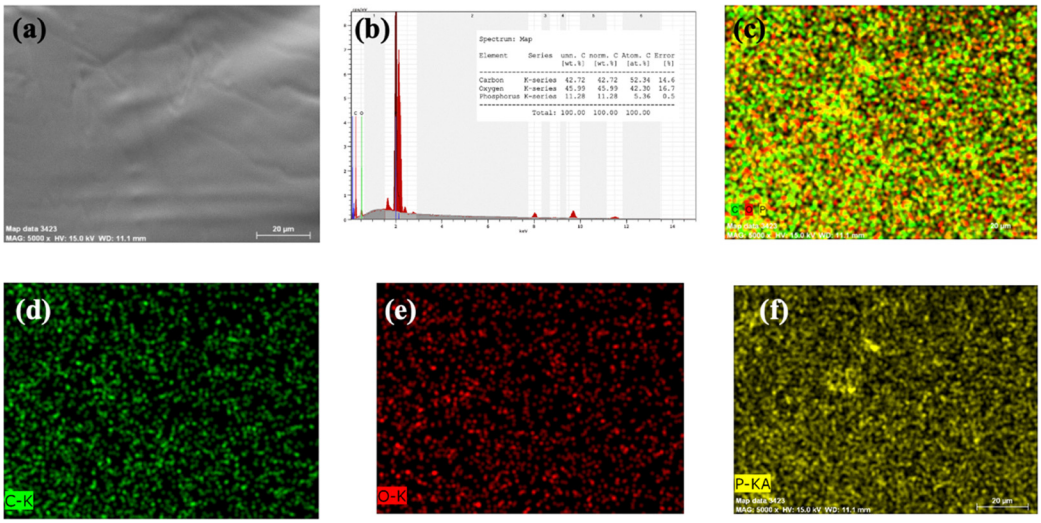

Fig. 3 P-CQDs (a) Representative SEM image, (b) EDX model, (c) EDX colour mapping and (d)–(f) EDX mapping images.

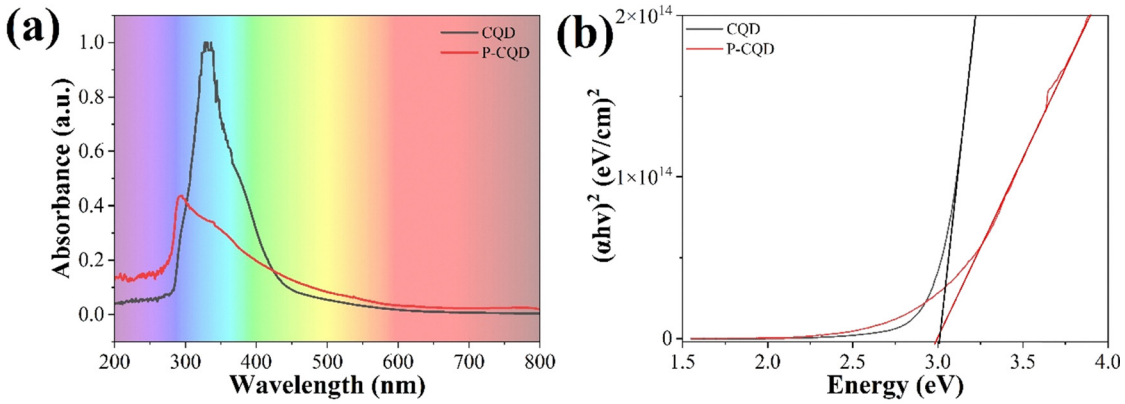

Fig. 4 (a) UV-vis spectrum and (b) band gap plots of the synthesized quantum dots.

surface chemistry that has been enriched, and that they demonstrate considerable potential in terms of electronic structure modification and defect passivation.[31]

Fig. 4a and b present the UV-vis absorption spectra and corresponding optical bandgap plots of the synthesized quantum dots, respectively. As shown in Fig. 4a, the CQDs exhibit an absorption peak at 330 nm, whereas the P-CQDs show a blue-shifted peak at 291 nm. Additionally, the P-CQDs demonstrate enhanced absorbance in the visible region. The optical bandgaps were determined from Tauc plots, as illustrated in Fig. 4b. The CQDs exhibit a bandgap of 3.01 eV, while the P-CQDs show a slightly reduced bandgap of 2.98 eV. It is worth noting that the bandgap of CQDs reported in the literature varies significantly depending on synthesis methods and particle size, with values ranging from 3.73 eV[41] to 2.50 eV.[42] This marginal decrease in bandgap suggests a modification of the electronic structure upon phosphorus doping.

3.2. Electrical properties

When exposed to light, charge carriers generated through photonic excitation (electrons and holes) arise from both intrinsic and impurity-related absorption mechanisms. These photoexcited carriers alter the conductivity of the semiconductor. Upon application of an external bias, the carriers drift toward the respective electrodes, where they are collected, producing a measurable photocurrent in the output circuit.[43] Current–voltage (I–V) measurements were performed at room temperature under varying light intensities. CQD-based photodetectors exhibited a noticeable increase in reverse current under reverse bias conditions. The observed rise in leakage current in the reverse polarity region (Fig. 5a and b) confirms that the fabricated photodetector efficiently supports photogeneration processes and demonstrates high sensitivity to incident light.[44] Furthermore, an enhancement in reverse bias current was observed under illumination intensities of 20 mW cm^{-2} and 100 mW cm^{-2}, although this increase was limited in magnitude.

A direct comparison in dark and illuminated conditions (100 mW cm^{-2}) is presented in Fig. 5c and d, respectively. Under dark conditions, the phosphorous-doped CQD-based photodetectors exhibited a significantly higher forward bias current compared to undoped CQDs/n-Si devices. Upon illumination, both reverse and forward currents in the heteroatom-doped CQDs/n-Si devices increased substantially relative to the undoped CQDs/n-Si device. This behavior highlights the role of phosphorous doping in enhancing photocarrier generation and transport efficiency, ultimately improving the optoelectronic performance of the photodetector.

The diode's ideality factor, barrier height, and series resistance were evaluated using thermionic emission theory, complemented by Cheung's and Norde's analytical approaches. The ideality factor (n) serves as a fitting parameter that adjusts the theoretical I–V relationship to align with the slope observed in experimental log(I)–V data. While an ideal diode has n = 1, practical Schottky barrier diodes often exhibit higher values due to factors such as bias-induced barrier height modification.[45] The barrier height (Φ_B) represents the energy difference between the metal's Fermi level and the conduction or valence band edge of the semiconductor, depending on the dominant carrier type.[46] Series resistance (R_s), which becomes more prominent at high forward bias, is another important parameter affecting device performance.[47] The calculated parameters are given Table 1.

Using the thermionic emission method, ideality factor and barrier height values for fabricated devices were determined under dark conditions. While ideality factor values were found as 3.24 and 3.55 for CQD/n-Si and P-CQD/n-Si devices, barrier heights values were as 0.670 and 0.593 eV, respectively. Deviations of n from unity can be attributed to R_s, non-uniform interface formation, and barrier inhomogeneity.[48,49]

The rectifying ratio (RR), a key indicator of photodetector electrical performance, was calculated at ±3 V for all device. RR plots of CQD/n-Si and P-CQD/n-Si devices are given in Fig. 6a and d, respectively. The CQD/n-Si device exhibited RR values of 2.60, 12.66, 14.32, 16.17, 16.92, and 18.59 at illumination intensities of 0, 20, 40, 60, 80, and 100 mW cm^{-2}, respectively. The P-CQD/n-Si device exhibited RR values of 4.99, 1.17, 0.70, 0.49, 0.37, and 0.29 at illumination intensities of 0, 20, 40, 60, 80, and 100 mW cm^{-2}, respectively. The reduced RR in the dark is due to the limited forward current, while illumination enhances forward current, improving rectification behavior.

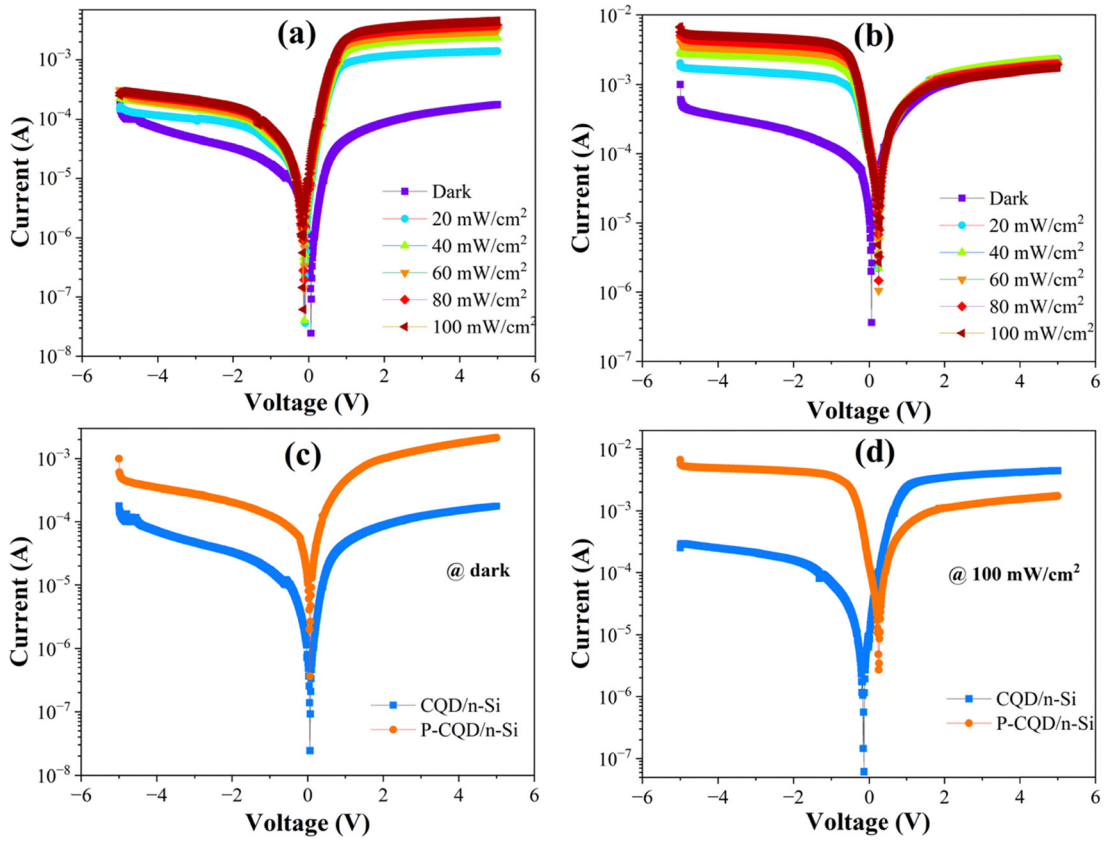

Fig. 5 Ln I–V plots of (a) CQD/n-Si and (b) P-CQD/n-Si. Comparison of Ln I–V plots of device under (c) dark and (d) 100 mW cm^{-2} condition.

Table 1 Electrical parameters

Device	Saturation current (I_0)	n (I–V)	n Cheung	Φ_b (I–V) (eV)	Φ_b Cheung (eV)	Φ_b Norde (eV)	R_s Cheung (kΩ ($H(I)$))	R_s Cheung ((kΩ ($d\ln(I)$))	R_s Norde (kΩ)
CQD/n-Si	1.27×10^{-7}	3.24	3.09	0.670	0.692	0.709	6.865	7.324	19.549
P-CQD/n-Si	2.55×10^{-6}	3.55	3.52	0.593	0.600	0.639	1.300	1.490	1.270

Among all devices, only the undoped CQD/n-Si shows improved rectification ratio with illumination, while doped devices suffer reduced performance due to increased reverse leakage under light.

Electrical parameters were further extracted using the Cheung method. dV/d ln I–I and $H(I)$–I plots of CQD/n-Si and P-CQD/n-Si devices are given in Fig. 6b and e, respectively. While ideality factor values were 3.09 and 3.52 for CQD/n-Si and P-CQD/n-Si devices, the barrier height values were 0.692 and 0.600 eV, respectively. Series resistance values from Cheung analysis were 6.865 and 7.324 kΩ for CQD/n-Si and 1.300 and 1.490 kΩ for P-CQD/n-Si. The Cheung analysis shows that CQD/n-Si has the highest series resistance (6.865–7.324 kΩ), while P-CQD/n-Si has the lowest (1.300–1.490 kΩ); overall, doping significantly reduces series resistance compared to the undoped device. The Norde method was also applied for cross-validation (Fig. 6c and f). Barrier height values were 0.709 and 0.639 eV for CQD/n-Si and P-CQD/n-Si devices, respectively, while series resistances were 19.549 and 1.270 kΩ.

3.3. Optoelectronic properties

The photocurrent response of a photodevice that varies with time can be assessed by conducting current–time (I–t) measurements under intermittent light exposure, using either an applied bias or in a self-powered configuration. This research evaluated the photocurrent response under self-powered conditions with different solar light intensities. Fig. 7a and c present the I–t properties of CQD/n-Si and P-CQD/n-Si devices, respectively. Both devices show a quick and instant rise in photocurrent when exposed to light, reflecting swift photoresponse characteristics. The photocurrent also increases gradually as light intensity rises, confirming the devices' responsiveness to varying light power densities. Fig. 7b and d further illustrate the rise and fall times under 100 mW cm^{-2} illumination, which are essential for assessing the response

speed of photodetectors. The rise time refers to the duration required for the photocurrent to increase from 10% to 90% of its peak value when illuminated, while the fall time represents the time for it to decrease from 90% to 10% once the light

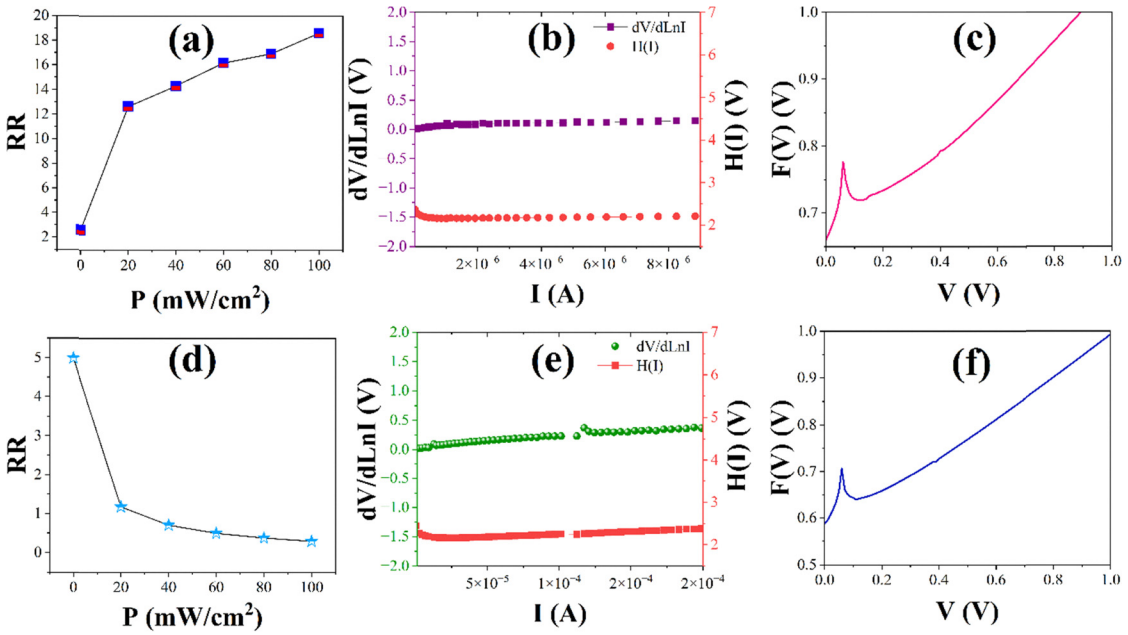

Fig. 6 (a) RR, (b) Cheung, and (c) Norde plots of CQD/n-Si. (d) RR, (e) Cheung, and (f) Norde plots of P-CQD/n-Si.

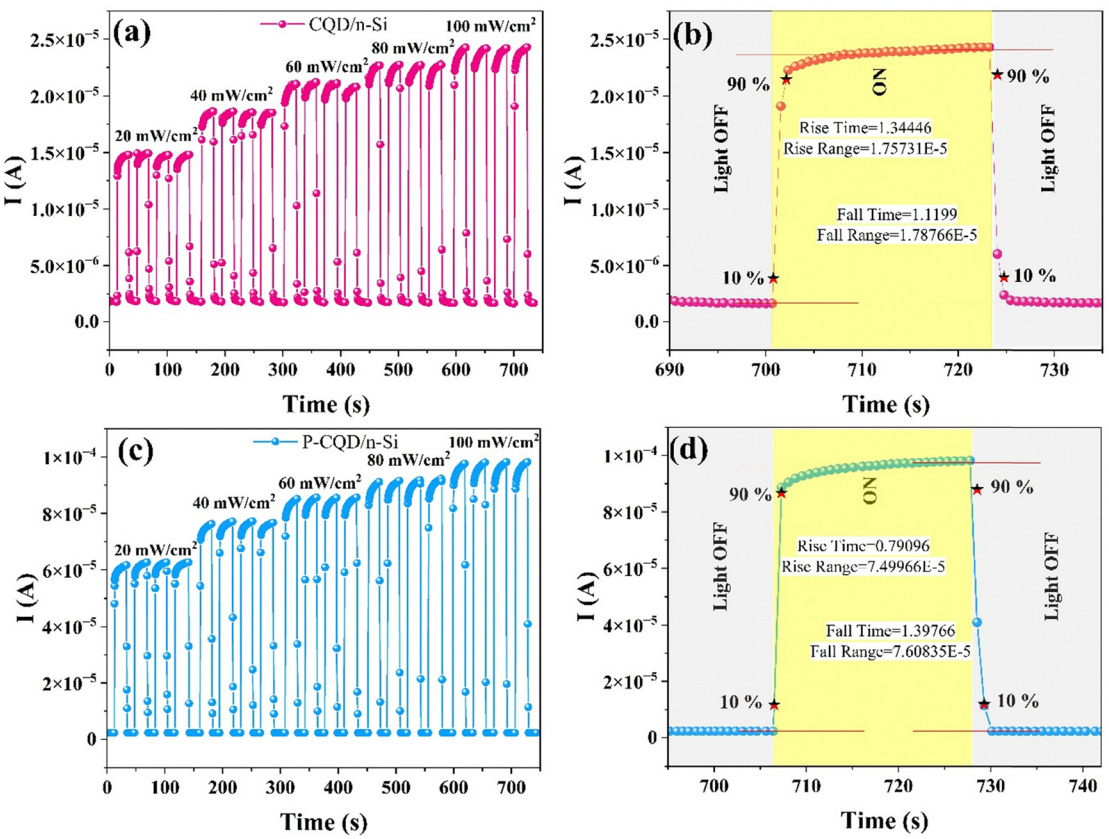

Fig. 7 (a) *I*–*t* and (b) Rise/fall time plots of CQD/n-Si. (c) *I*–*t* and (d) Rise/fall time plots of P-CQD/n-Si.

source is turned off. These temporal response characteristics—rise and fall times—are key indicators of a device's sensitivity and suitability for rapid photodetection applications.

The transient photoresponse measurements under varying illumination intensities (20–100 mW cm^{-2}) exhibit clear and repeatable on–off switching behavior, indicating stable and reversible photodetection characteristics. In all cases, the photocurrent increases stepwise with higher light intensity, with P-CQD/n-Si producing the highest absolute photocurrent, followed by the undoped CQD/n-Si device. The rise and fall times differ slightly between these devices: CQD/n-Si exhibits a rise time of 1.344 s and a fall time of 1.119 s, while P-CQD/n-Si shows a short rise time of 0.791 s and a fall time of 1.398 s, indicating a rapid photoresponse and efficient carrier dynamics. Overall, the results demonstrate that phosphorus doping enhances photocurrent generation and maintains fast response behavior, making the P-CQD/n-Si structure a promising candidate for high-speed and high-sensitivity photodetection applications.

The main factors that influence the effectiveness of a photodetector are photocurrent (I_p), photosensitivity (K), responsivity (R), noise equivalent power (NEP), and specific detectivity (D^*). These traits are derived using the subsequent formulas:[50,51]

$$I_p = I_{light} - I_{dark} \quad (1)$$

$$K = \frac{I_p}{I_{dark}} \quad (2)$$

$$R = \frac{I_p}{PA} \quad (3)$$

$$NEP = \frac{\sqrt{2e\, I_{dark}}}{R} \quad (4)$$

$$D^* = \frac{\sqrt{A}}{NEP} \quad (5)$$

In this context, P signifies the power density of the incident light, while A denotes the effective area of the photodetector. Responsivity (R) measures the efficiency with which the device transforms optical input into electrical output. Photosensitivity (K) represents the ratio of photocurrent to dark current, demonstrating the device's sensitivity to light. NEP denotes the least optical power detectable above the noise threshold, acting as an essential standard for photodetector sensitivity. Specific detectivity (D^*) quantifies a device's capability to identify faint optical signals, and it is standardized to the area and bandwidth of the detector. As shown in Fig. 8a–f and outlined in Table 2, we determined and graphed these performance metrics for each light intensity level to assess the general photodetection capabilities of the devices. Fig. 8a illustrates the photocurrent plots under various light intensities. The photocurrent increases with illumination intensity for all devices, though the magnitude varies between them. The CQD/n-Si device shows a steady rise from 1.27×10^{-5} A at 20 mW cm^{-2} to 2.22×10^{-5} A at 100 mW cm^{-2}. In contrast, the P-CQD/n-Si device exhibits substantially higher photocurrents, starting at 6.07×10^{-5} A and reaching 9.66×10^{-5} A, indicating enhanced photocarrier generation efficiency and effective light absorption.

Fig. 8b presents the photosensitivity plots under different illumination intensities. The CQD/n-Si device starts at a photosensitivity of 6.85 and increases consistently to 11.96 with higher illumination, reflecting a gradual improvement in photoresponse. The P-CQD/n-Si device, however, records a much higher initial sensitivity of 60.70 and maintains strong performance, reaching 96.60 at the highest illumination level.

Fig. 8c shows the responsivity behavior as a function of illumination intensity. Responsivity decreases for both devices with increasing illumination, a typical outcome of saturation effects at high light intensities. The CQD/n-Si device decreases from 0.081 A W^{-1} to 0.028 A W^{-1}, while P-CQD/n-Si demonstrates significantly higher values, dropping from 0.386 A W^{-1} to 0.123 A W^{-1} as illumination increases. This result confirms the superior light-to-current conversion efficiency of the P-CQD/n-Si structure, especially at lower intensities.

Fig. 8d illustrates the noise equivalent power (NEP) variation with illumination. NEP values rise with increasing light intensity for both devices, reflecting higher noise levels under stronger illumination. The CQD/n-Si device shows a pronounced NEP increase from 9.51×10^{-12} to 2.72×10^{-11} W $Hz^{-1/2}$, while the P-CQD/n-Si device maintains the lowest NEP overall, ranging from 1.46×10^{-12} to 4.60×10^{-12} W $Hz^{-1/2}$, confirming its superior low-noise and high-detection capability.

Fig. 8e depicts the detectivity behavior at different illumination intensities. Detectivity decreases for all samples with increasing light intensity, consistent with the rise in noise and dark current under strong illumination. The CQD/n-Si device shows a decline from 1.47×10^{10} Jones to 5.12×10^{9} Jones, while the P-CQD/n-Si device exhibits the highest detectivity, decreasing from 6.99×10^{10} to 2.22×10^{10} Jones. These results demonstrate that phosphorus doping significantly enhances sensitivity, responsivity, and detectivity, making the P-CQD/n-Si device a promising candidate for high-performance, low-noise photodetection applications.

The electrical performance of the device is not only limited by the Schottky barrier height but is also directly related to the defect density at the interface and the carrier recombination dynamics. The deviation of the ideality factor observed in the conventional I–V characteristics from 1 (3.24 for CQD/n-Si, 3.55 for P-CQD/n-Si) indicates that the transport mechanism shifts from pure thermionic emission to trap-assisted recombination and space charge-limited current (SCLC) regimes.

In unmodified CQD layers, the dense deep-level traps created by the functional groups on the surface cause carriers to be trapped at the interface and increase non-radiative recombination losses. Phosphorus doping passivates these surface states *via* C–P and C–O–P bond configurations. Doping dynamically lowers the electron injection barrier by bringing the Fermi level closer to the conduction band (strengthening the n-type character). This is the key factor explaining the increase in I_{ph}. The use of P-CQD can be attributed to minimizing the voltage-dependent interface state density value by causing the

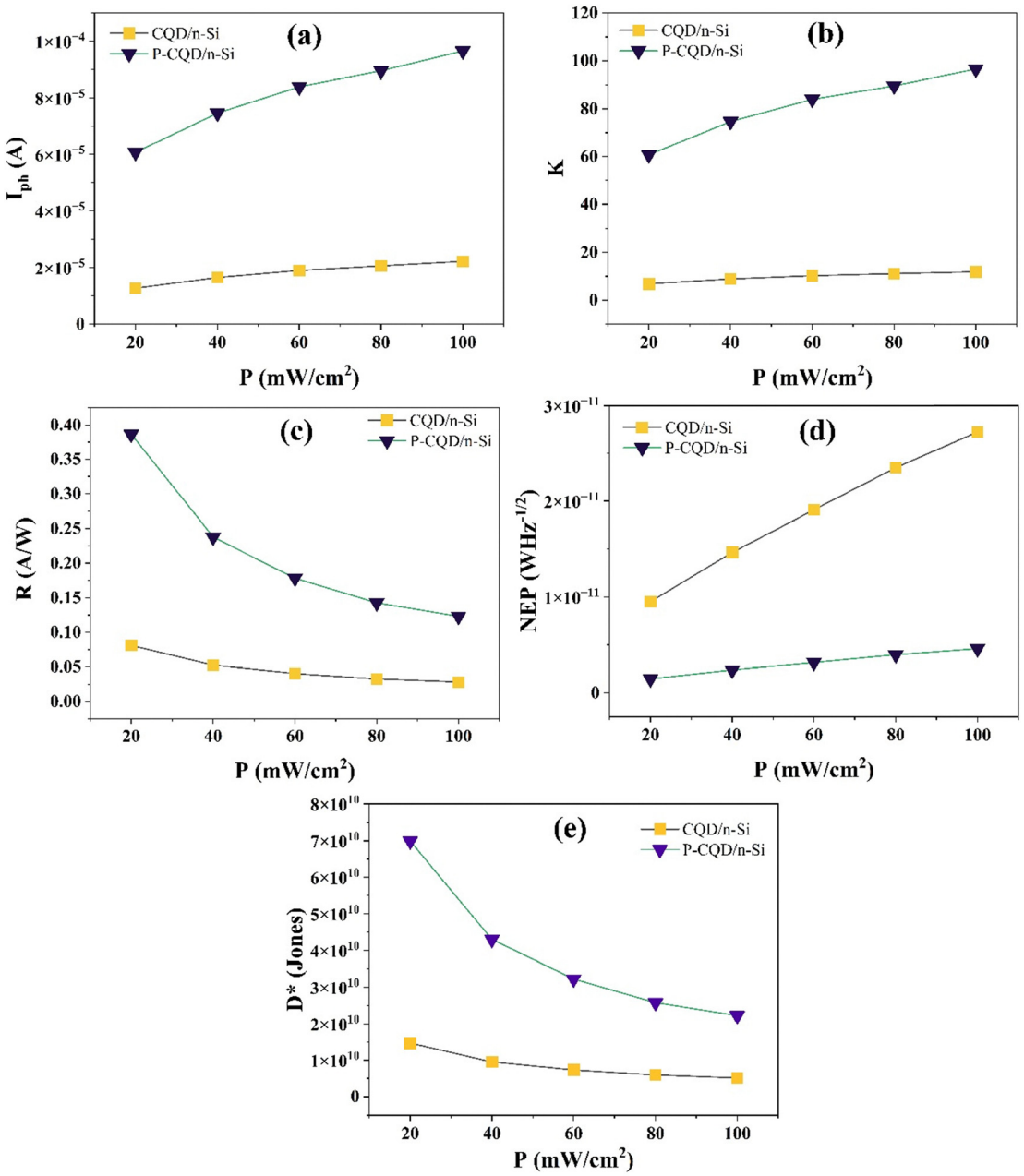

Fig. 8 (a) photocurrent, (b) photosensitivity, (c) responsivity, (d) NEP, and (e) detectivity plots of the devices.

Table 2 Photodetector parameters under various solar light intensities

Device	Power (mW cm^{-2})	Photocurrent (A)	Photosensitivity -	Responsivity (A W^{-1})	Detectivity (Jones)	NEP (WHz$^{-1/2}$)
CQD/n-Si	20	1.27×10^{-5}	6.85	0.081	1.47×10^{10}	9.51×10^{-12}
	40	1.65×10^{-5}	8.89	0.053	9.52×10^{9}	1.47×10^{-11}
	60	1.90×10^{-5}	10.24	0.040	7.31×10^{9}	1.91×10^{-11}
	80	2.06×10^{-5}	11.10	0.033	5.94×10^{9}	2.35×10^{-11}
	100	2.22×10^{-5}	11.96	0.028	5.12×10^{9}	2.72×10^{-11}
P-CQD/n-Si	20	6.07×10^{-5}	60.70	0.386	6.99×10^{10}	1.46×10^{-12}
	40	7.47×10^{-5}	74.70	0.238	4.30×10^{10}	2.38×10^{-12}
	60	8.40×10^{-5}	84.00	0.178	3.22×10^{10}	3.17×10^{-12}
	80	8.96×10^{-5}	89.60	0.143	2.58×10^{10}	3.97×10^{-12}
	100	9.66×10^{-5}	96.60	0.123	2.22×10^{10}	4.60×10^{-12}

formation of a more homogeneous dipole layer at the interface. This passivation effect suppresses the dark current, especially in low-voltage regions, and increases the specific detectivity (D^*) of the photodetector to the level of 10^{10} Jones. Phosphorus doping creates an electric dipole moment in the CQD layer. This vacuum level shift facilitates the movement of photogenerated holes from n-Si towards the anode, while ensuring that electrons are collected before reaching recombination centers.

The enhancement in performance cannot be ascribed exclusively to the straightforward doping effect of CQDs; instead, it originates from the modulation of the electronic structure engendered by phosphorus doping and the consequent enhancement in interfacial properties. In particular, the process of phosphorus doping has been shown to create surface states that enhance charge transport efficiency. Concurrently, this process also results in the passivation of defect sites at the interface. This dual effect plays a critical role in suppressing trap-assisted recombination pathways and extending carrier lifetime. Furthermore, the significant increase observed in optoelectronic parameters such as photocurrent, responsivity and detectivity indicates that P-CQDs both reduce non-radiative recombination losses in the device and facilitate more efficient collection of charge carriers. The present findings demonstrate unequivocally that phosphorus-doped CQDs act not only as structural regulators but also as active electronic regulators within the device architecture. In this context, the present study goes beyond the scope of heteroatom doping approaches to reveal the mechanistic relationship between doping and electronic structure modification, as well as its impact on macroscopic device performance. This approach facilitates the more rational design of interface materials for high-performance optoelectronic systems. The results obtained demonstrate that the process of phosphorus doping not only enhances optical absorption but also improves both photon carrier generation and interfacial charge transport in a synergistic manner.

Fig. 9a–c presents the wavelength-dependent photocurrent responses of the Ag/n-Si/Al, Ag/CQD/n-Si/Al, and Ag/P-CQD/n-Si/Al photodetectors, respectively, measured under zero-bias conditions. The devices were illuminated using a series of narrowband visible hard-coated band-pass filters (Thorlabs GmbH, Germany) with an average full width at half maximum (FWHM) of 10 nm. These filters span a wide spectral range from the ultraviolet (UV) to the visible and near-infrared (NIR) regions (351–1600 nm). This experimental setup allowed for a thorough assessment of the spectral response behavior of all three photodetectors. All devices exhibited broadband spectral sensitivity, with measurable photocurrent responses across the entire tested range. However, the Ag/P-CQD/n-Si/Al device (Fig. 9c) produced the highest photocurrent values under identical illumination conditions, followed by the Ag/CQD/n-Si/Al device (Fig. 9b), while the Ag/n-Si/Al device (Fig. 9a) showed the lowest response. The enhancement observed in the P-CQD/n-Si device is especially pronounced in the visible to NIR regions, suggesting improved light absorption and charge carrier separation due to surface passivation and optimized quantum dot properties.

The photocurrent trends for all devices generally peak within the visible range (around 600–900 nm), followed by a gradual decline toward longer wavelengths. A more pronounced decrease in photocurrent is observed beyond approximately 1100 nm, which can be attributed to reduced photon energy approaching and falling below the silicon bandgap, leading to less efficient electron–hole pair generation and increased recombination losses. The Ag/n-Si/Al device exhibits a comparatively weaker response throughout the spectrum, whereas the Ag/CQD/n-Si/Al device shows moderate improvement, and the Ag/P-CQD/n-Si/Al device demonstrates the strongest and most stable response. The extended near-infrared (NIR) response observed in our device, particularly under zero-bias operation, can be further understood in light of recent studies on silicon-based photodetectors employing plasmonic effects. In conventional Si photodetectors, the spectral response is fundamentally limited by the Si bandgap ($\sim$1.12 eV), restricting detection to wavelengths below $\sim$1100 nm. However, Zhang *et al.* demonstrate that localized surface plasmon resonance (LSPR) in metal nanostructures integrated with silicon can significantly extend the spectral response into the sub-bandgap NIR region.[52] In such systems, incident NIR photons excite collective oscillations of electrons in metallic nanostructures, leading to strong near-field enhancement and the generation of energetic (“hot”) electrons. These hot carriers can overcome the Schottky barrier at the metal–semiconductor interface and be injected into the silicon, producing a measurable photocurrent even for sub-bandgap photons.[53] All measurements were conducted under self-powered conditions (0 V applied bias), confirming the intrinsic photovoltaic behavior of these junctions. This zero-bias operation highlights their potential for low-power, broadband photodetector applications.

In current CQD/n-Si and P-CQD/n-Si devices, the self-powering process originates from the intrinsic electric field established at the metal-semiconductor interface upon Schottky contact formation. According to modern Schottky barrier concepts, the barrier height (Φ_B) is not only determined by the metal work function difference but is also greatly influenced by interface dipole formation and Fermi level stabilization effects resulting from interface coupling and charge redistribution. This leads to a stable energy barrier at the junction even in the absence of external bias. When an Ag top contact is placed on a CQD or P-CQD modified n-Si surface, charge transfer occurs across the interface, leading to the formation of an interface dipole layer. This dipole alters the local electrostatic potential and defines the effective Schottky barrier height. In parallel, the alignment of Fermi levels between the metal and the semiconductor creates a built-in potential, causing band bending in the n-Si region. This built-in potential establishes a depletion region near the interface where mobile charge carriers are exhausted and a strong internal electric field is established. Under illumination, electron–hole pairs formed by photogeneration in or near this depletion region are efficiently separated by this internal electric field.

Furthermore, we can say that phosphor doping in CQDs enhances this mechanism with two key effects. The first is ray

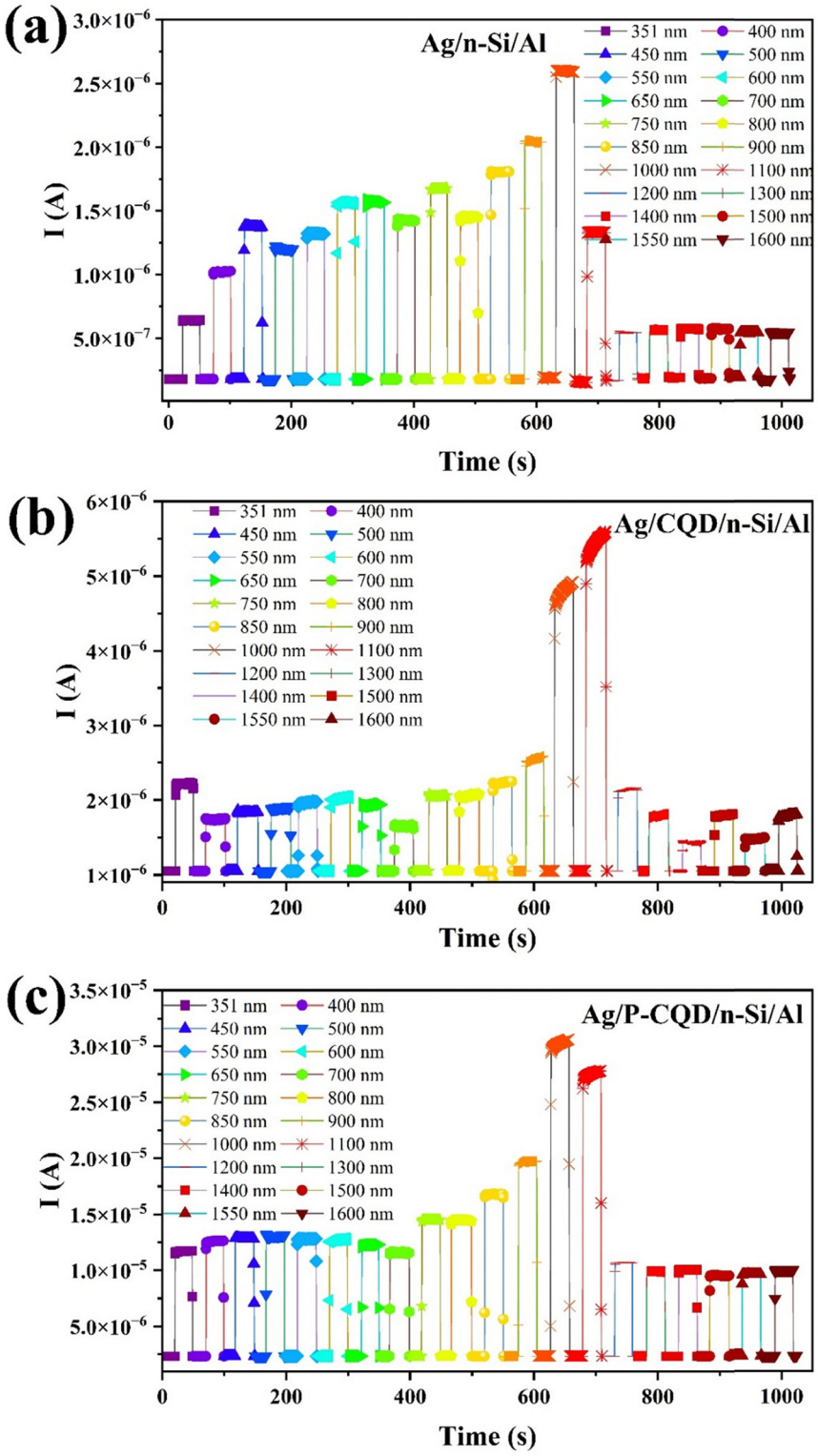

Fig. 9 *I*–*t* plots of (a) Ag/n-Si/Al, (b) Ag/CQD/n-Si/Al, and (c) Ag/P-CQD/n-Si/Al devices measured under various wavelengths.

dipole modulation, which slightly adjusts the effective barrier height and improves band alignment. The second is defect passivation, which reduces trap-assisted recombination at the interface. As a result, the P-CQD/n-Si device exhibits more efficient carrier separation and collection under zero-bias conditions, leading to significantly increased photocurrent and sensing capability compared to the undoped device.

Table 3 summarizes the spectral performance of the Ag/n-Si/Al, Ag/CQD/n-Si/Al, and Ag/P-CQD/n-Si/Al photodetectors across a wavelength range of 351–1600 nm under self-powered operation

Table 3 Main photodetector parameters under 351–1600 nm and zero bias

	Ag/n-Si/Al			Ag/CQD/n-Si/Al			Ag/P-CQD/n-Si/Al		
λ (nm)	R (mA W^{-1})	D^* (Jones)	EQE (%)	R (mA W^{-1})	D^* (Jones)	EQE (%)	R (mA W^{-1})	D^* (Jones)	EQE (%)
351	2.17	6.19×10^8	0.801	7.57	1.16×10^9	2.797	59.06	6.06×10^9	21.836
400	4.46	1.28×10^9	1.447	4.51	6.88×10^8	1.463	66.06	6.78×10^9	21.435
450	6.82	1.95×10^9	1.966	5.02	7.66×10^8	1.447	67.97	6.98×10^9	19.604
500	5.80	1.66×10^9	1.505	5.34	8.15×10^8	1.385	67.34	6.91×10^9	17.478
550	6.56	1.88×10^9	1.548	5.91	9.02×10^8	1.394	66.70	6.85×10^9	15.739
600	7.96	2.28×10^9	1.722	6.29	9.61×10^8	1.361	66.06	6.78×10^9	14.290
650	8.15	2.33×10^9	1.628	5.59	8.54×10^8	1.116	62.88	6.46×10^9	12.555
700	7.13	2.04×10^9	1.323	3.93	6.01×10^8	0.730	60.33	6.19×10^9	11.186
750	8.79	2.51×10^9	1.521	6.53	9.97×10^8	1.129	78.16	8.03×10^9	13.526
800	7.45	2.13×10^9	1.209	6.29	9.61×10^8	1.021	77.53	7.96×10^9	12.577
850	9.55	2.73×10^9	1.459	7.44	1.14×10^9	1.136	92.18	9.46×10^9	14.074
900	10.83	3.10×10^9	1.561	9.48	1.45×10^9	1.367	110.65	1.14×10^{10}	15.956
1000	14.65	4.19×10^9	1.901	23.93	3.66×10^9	3.106	176.25	1.81×10^{10}	22.875
1100	6.56	1.88×10^9	0.774	28.33	4.33×10^9	3.343	160.33	1.65×10^{10}	18.917
1200	1.59	4.55×10^8	0.172	6.93	1.06×10^9	0.749	53.32	5.47×10^{10}	5.767
1300	1.70	4.74×10^8	0.170	4.64	7.08×10^8	0.463	48.86	5.02×10^9	4.878
1400	1.72	4.37×10^8	0.159	2.60	3.97×10^8	0.241	50.14	5.15×10^9	4.648
1500	1.66	4.01×10^8	0.143	4.89	7.47×10^8	0.423	46.13	4.74×10^9	3.991
1550	1.59	3.83×10^8	0.133	2.72	4.16×10^8	0.228	47.97	4.93×10^9	4.017
1600	1.45	3.64×10^8	0.118	4.76	7.27×10^8	0.386	47.98	4.93×10^9	3.892

(0 V bias). The data were derived from measured photocurrents using narrow band-pass filters and used to calculate key photodetection metrics. The photocurrent increases significantly with wavelength-dependent illumination intensity for all devices. The Ag/P-CQD/n-Si/Al photodetector produces the highest photocurrent values, reaching 2.77×10^{-5} A at 1000 nm, which is an order of magnitude larger than the undoped Ag/CQD/n-Si/Al device, peaking at 4.45×10^{-6} A at 1100 nm. In comparison, the Ag/n-Si/Al device exhibits much lower photocurrent, with a maximum of 2.3×10^{-6} A at 1000 nm, confirming that phosphorus doping greatly enhances light absorption and carrier generation efficiency.

The photosensitivity (K) of the devices also varies with wavelength. The Ag/CQD/n-Si/Al photodetector achieves a maximum value of 4.23 at 1100 nm, while the Ag/P-CQD/n-Si/Al device maintains higher and more stable sensitivity across the measured range, with K values between approximately 3.1 and 11.88. In contrast, the Ag/n-Si/Al device shows lower sensitivity, increasing from 1.13 at 351 nm to 7.67 at 1000 nm, followed by a decrease at longer wavelengths. This demonstrates that Ag/P-CQD/n-Si/Al not only generates a higher absolute photocurrent but also retains stronger relative light-to-dark current performance.

In terms of responsivity (R), Ag/P-CQD/n-Si/Al again outperforms the undoped device, achieving values as high as 0.176 A W^{-1} at 1000 nm under zero bias, while Ag/CQD/n-Si/Al reaches a maximum of approximately 0.028 A W^{-1}. The Ag/n-Si/Al device shows significantly lower responsivity, with a peak value of 0.0146 A W^{-1} at 1000 nm, confirming the superior light-to-current conversion efficiency of the phosphorus-doped device.

The noise-equivalent power (NEP) results show that lower NEP values correspond to higher sensitivity. Ag/P-CQD/n-Si/Al exhibits the lowest NEP values, with a minimum of 4.90×10^{-12} W Hz$^{-1/2}$, while Ag/CQD/n-Si/Al shows higher values around 2.05×10^{-11} W Hz$^{-1/2}$. In contrast, the Ag/n-Si/Al device presents higher NEP values, with a minimum of 2.11×10^{-11} W Hz$^{-1/2}$ at 1000 nm and increasing further in the infrared region, emphasizing the superior noise performance of the phosphorus-doped device.

Detectivity (D^*) follows a similar trend. Ag/P-CQD/n-Si/Al achieves the highest detectivity, reaching 1.81×10^{10} Jones at 1000 nm, compared to 4.33×10^9 Jones for Ag/CQD/n-Si/Al at 1100 nm. The Ag/n-Si/Al device shows lower detectivity, with a maximum of 4.19×10^9 Jones at 1000 nm, indicating comparatively weaker noise-limited performance.

Finally, the external quantum efficiency (EQE) of the Ag/P-CQD/n-Si/Al device shows a remarkable enhancement, exceeding 20% in several spectral regions with a peak of approximately 22.88%. In contrast, Ag/CQD/n-Si/Al reaches a maximum EQE of about 3.34%, while the Ag/n-Si/Al device exhibits much lower efficiency, with a maximum of ~1.90% at 1000 nm. This demonstrates that phosphorus incorporation significantly improves photon-to-charge conversion, resulting in stronger light-harvesting and more efficient charge transport.

Overall, the P-CQD/n-Si photodetector exhibits superior broadband sensitivity, higher responsivity, enhanced detectivity, and markedly improved quantum efficiency compared to both the undoped CQD/n-Si and the Ag/n-Si/Al devices. These findings confirm that phosphorus doping not only strengthens light absorption but also facilitates more efficient carrier separation and collection, making Ag/P-CQD/n-Si/Al a highly promising material for next-generation self-powered photodetectors operating across the UV–NIR spectral range.

Table 4 presents a comparative analysis of responsivity, detectivity, and self-powered operation of various QD-based photodetectors reported in the literature alongside the present work. It can be observed that several previously reported devices exhibit high responsivity and detectivity; however, many of them operate under an applied bias, such as CQD-based devices showing R = 125 A W^{-1} and $D^* = 4.73 \times 10^{13}$ Jones at −0.4 V,[54] and CQDs/ZnO structures with $D^* = 8.33 \times 10^{12}$ Jones

Table 4 Comparison of photodetectors reported in the literature and the present work

Interlayer	λ (nm)	R (A W^{-1})	D^* (Jones)	Applied Bias (V)	Ref.
CQD	1550	125	4.73×10^{13}	−0.4	54
CQDs/ZnO	365	—	8.33×10^{12}	−2	55
CQDs/ZnO	365	—	3.27×10^{8}	0	56
CQD/Si	352	0.2846	1.55×10^{13}	0	58
	580	0.6452	3.53×10^{13}		
	850	0.3891	2.12×10^{13}		
ZnO:CQDs	525	—	2.46×10^{11}	0	57
ZnO QDs-P3HT	360	0.00304	8.76×10^{7}	0	59
P-CQD	351	0.05906	6.06×10^{9}	0	This
	550	0.06670	6.85×10^{9}		study
	1000	0.17625	1.81×10^{10}		

at −2 V.[55] In contrast, self-powered devices operating at 0 V typically demonstrate lower performance metrics, as seen in CQDs/ZnO (D^* = 3.27 × 10^8 Jones)[56] and ZnO:CQDs systems (D^* = 2.46 × 10^{11} Jones).[57] Notably, dual-sized CQD/Si devices have shown relatively high detectivity up to 3.53 × 10^{13} Jones at 0 V,[58] highlighting the advantage of silicon-based heterojunctions. In comparison, the P-CQD-based device in this study demonstrates responsivity values ranging from 0.059 to 0.176 A W^{-1} and detectivity up to 1.81 × 10^{10} Jones under self-powered conditions. Although the performance is lower than biased devices, it is competitive among self-powered photodetectors, confirming the effectiveness of phosphorus doping in enhancing charge separation and interfacial charge transfer without the need for external bias. These results indicate that the present device offers a promising balance between performance and energy-efficient operation.

Although FTIR and EDX analyses confirm the successful incorporation and homogeneous distribution of phosphorus within the CQD matrix, a precise quantitative determination of the absolute doping concentration was not performed in this study. This limitation is attributable to the inherent challenges associated with accurately quantifying low-level heteroatom incorporation in carbon-based nanostructures using conventional characterization techniques. However, it is well established in the literature that even relatively low concentrations of heteroatom dopants can induce significant modifications in the electronic structure of CQDs, leading to the formation of localized states, interfacial dipoles, and charge redistribution effects. These changes have a significant impact on the dynamics of carrier transport and recombination at the device interface. In the present work, the observed enhancement in photocurrent, responsivity, and detectivity for P-CQD/n-Si devices suggests that the achieved doping level lies within an effective regime that optimizes interfacial charge transfer without introducing excessive defect-mediated recombination centers. A systematic study involving controlled variation of phosphorus concentration would be highly valuable in establishing a quantitative relationship between dopant level and device performance.

3.4. Stability and repeatability analysis

Stability and repeatability measurements were conducted at the wavelength corresponding to the highest responsivity. The devices were stored at room temperature. Current–transient measurements of CQD/n-Si devices taken on day 0 and after 20 days are shown in Fig. 10a and b, respectively, while the corresponding rise/fall time plot is presented in Fig. 10c. On the first day of measurement, CQDs/n-Si devices exhibited notably higher photocurrent values, with I_{ph} increasing from 4.47 × 10^{-6} A for 1 cycle to 4.93 × 10^{-6} A after 50 cycles. Correspondingly, the responsivity improved from 0.02846 A W^{-1} to 0.03139 A W^{-1}, while photosensitivity also increased slightly from 4.246 to 4.683.

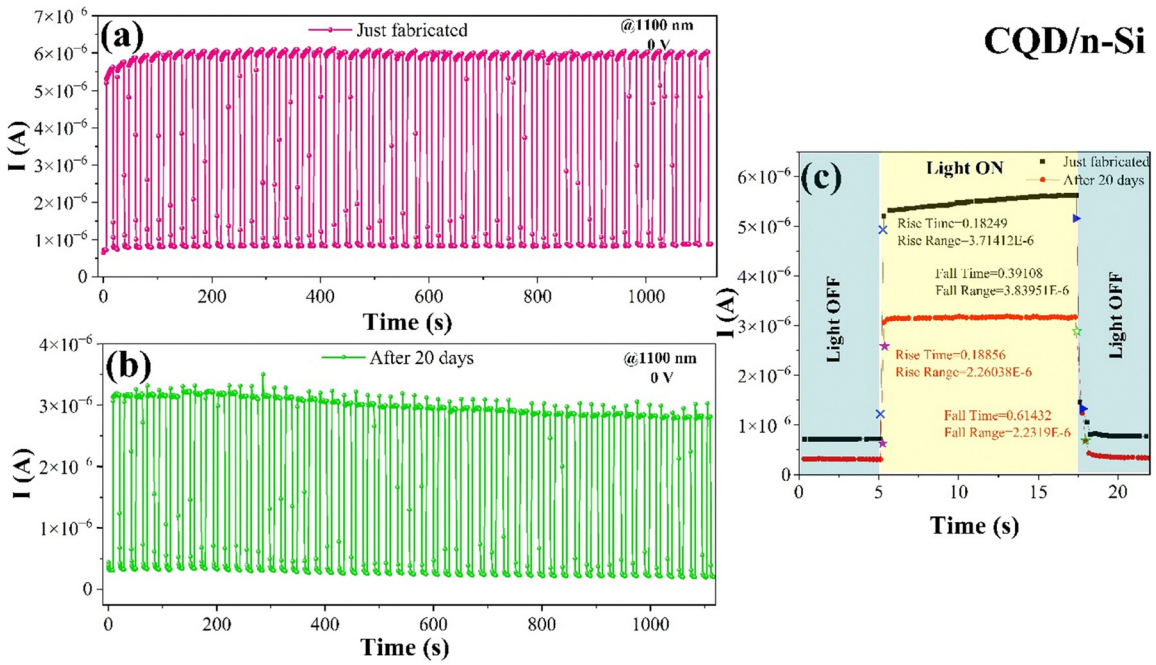

Fig. 10 I–t plots of CQD/n-Si at (a) first days and (b) after 20 days. (c) Rise/fall time plots.

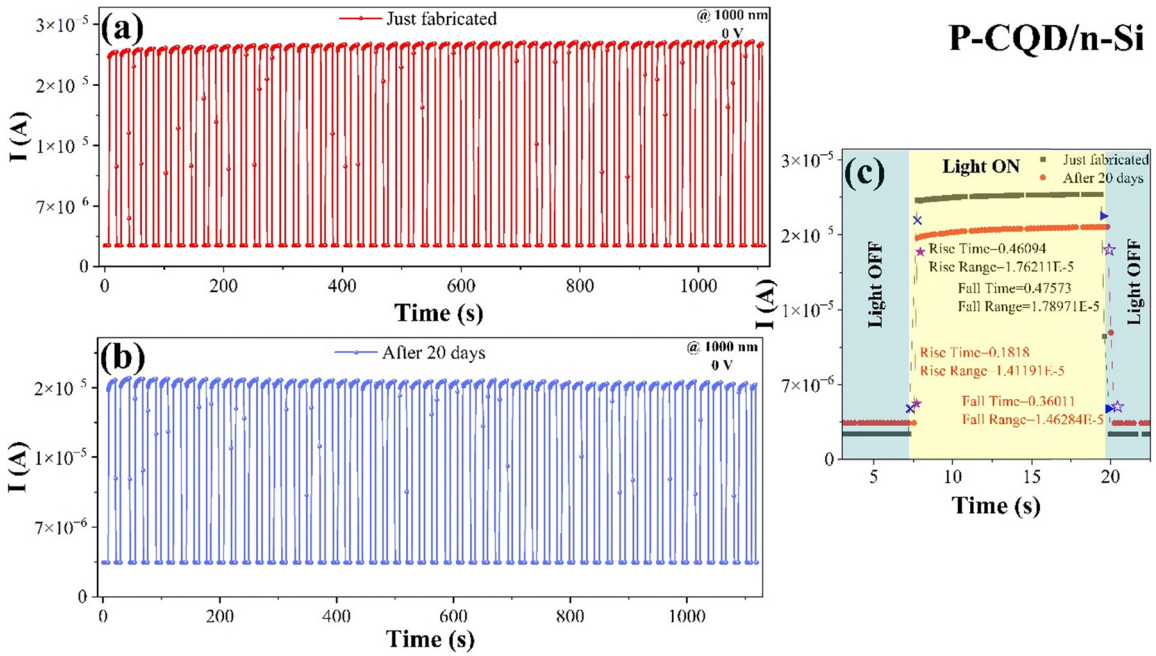

Fig. 11 *I*–*t* plots of P-CQD/n-Si at (a) first days and (b) after 20 days. (c) Rise/fall time plots.

Detectivity values were high, measured at 4.35×10^9 and 4.79×10^9 Jones for 1 and 50 cycles, respectively, indicating stable and slightly enhanced performance with repeated cycling. After 20 days of aging, the device performance decreased noticeably. The photocurrent dropped to 2.72×10^{-6} A for 1 cycle and further to 2.42×10^{-6} A after 50 cycles. Similarly, responsivity declined from 0.01732 A W^{-1} to 0.01541 A W^{-1}, and photosensitivity fell from 6.800 to 6.050. Detectivity also decreased from 4.29×10^9 to 3.82×10^9 Jones. Moreover, EQE values decreased from 3.343 to 2.044% after 20 days. Rise time and fall time for as-fabricated device were as 0.182 and 0.391 s, respectively. After 20 days, the rise time and fall time increased to 0.188 and 0.614 s, respectively.

Current–transient measurements of P-CQD/n-Si devices taken on day 0 and after 20 days are shown in Fig. 11a and b, respectively, while the corresponding rise/fall time plot is presented in Fig. 11c. P-CQD/n-Si devices outperformed all other groups, with fresh samples exhibiting exceptionally high I_{ph} ($\sim 2.3 \times 10^{-5}$ A), responsivities > 0.14 A W^{-1}, and detectivities exceeding 1.48×10^{10} Jones. Even after 20 days, they maintained strong performance, with responsivity still above 0.115 A W^{-1} and detectivity close to 1.0×10^{10} Jones, highlighting remarkable stability and superior optoelectronic properties. The EQE decreased from 22.875 to 15.211% after 20 days. Rise time and fall time for as-fabricated device were as 0.460 and 0.475 s, respectively. After 20 days, the rise time and fall time decreased to 0.181 and 0.360 s, respectively.

4. Conclusion

This study systematically elucidates the impact of phosphorus heteroatom doping on the structural, optical, electrical, and optoelectronic properties of carbon quantum dot-based Schottky photodetectors. Phosphorus incorporation into the carbon framework resulted in surface defect passivation, redistribution of charge density, and formation of new energy states that enhanced photon absorption and stabilized radiative recombination pathways. Structural analyses confirmed homogeneous nanostructures with preserved morphology after doping, while spectroscopic results demonstrated improved emission stability and broadened absorption characteristics. Electrical characterization revealed that P-CQD/n-Si heterojunctions exhibit reduced Schottky barrier height and markedly lower series resistance compared to undoped CQD devices, indicating improved metal–semiconductor interface alignment and enhanced carrier transport. Although rectification ratio behavior varied under illumination due to increased reverse leakage currents, the overall photodetection performance was substantially enhanced in doped devices. It is important to note that the enhancement in device performance observed cannot be attributed solely to a compositional modification. Rather, it originates from phosphorus-induced modulation of the electronic structure and interfacial energetics. Phosphorus doping introduces localized surface states that facilitate efficient charge transfer while simultaneously passivating defect sites. This process suppresses trap-assisted recombination pathways and extends carrier lifetime. This dual functionality establishes a direct link between doping-induced electronic structure engineering and macroscopic device performance. Optoelectronic investigations under self-powered conditions demonstrated that phosphorus doping significantly improves photocurrent generation, photosensitivity, responsivity, detectivity, and external quantum efficiency across a wide spectral range (UV-NIR). The P-CQD/n-Si device consistently outperformed the undoped

structure, achieving high detectivity on the order of 10^{10} Jones and EQE values exceeding 20%, particularly in the near-infrared region. Furthermore, long-term stability measurements confirmed that phosphorus-doped devices maintain strong operational reliability over time. The enhancements observed in the photodetection parameters further substantiate the efficacy of phosphorus doping in augmenting both charge separation efficiency and interfacial charge extraction, while concomitantly mitigating non-radiative recombination losses. Overall, phosphorus-doped carbon quantum dots provide an effective platform for interface engineering in Schottky-based optoelectronic systems. The synergistic enhancement of interfacial energetics, carrier transport, and broadband light harvesting demonstrates their strong potential for integration into next-generation self-powered photodetectors, high-speed optical switches, and advanced wide-band optoelectronic devices. This work represents an advancement beyond conventional heteroatom doping strategies by providing mechanistic evidence that links dopant-induced electronic structure modification with macroscopic device performance. This, in turn, offers a more rational framework for the design of high-performance optoelectronic materials. Subsequent research may concentrate on the correlation between dopant concentration and interfacial energetics, with a view to further optimising device performance.

Conflicts of interest

The authors have no relevant financial or non-financial interests to disclose.

Data availability

The data that support the findings of this study are available from the corresponding author upon reasonable request.

References

1 J. Singh, *Electronic and optoelectronic properties of semiconductor structures*, Cambridge University Press, 2007.
2 R. T. Tung, The physics and chemistry of the Schottky barrier height, *Appl. Phys. Rev.*, 2014, **1**(1), 011304, DOI: 10.1063/1.4858400.
3 Z. Xiang, J.-W. Luo and S.-S. Li, Unified interface dipole theory for Fermi level pinning effect at metal-semiconductor contacts, *arXiv*, preprint, 2025. https://arxiv.org/abs/2511.21494.
4 J.-Y. Wu, H.-Y. Jiang, Z.-Y. Wen and C.-R. Wang, Fundamental and Photodetector Application of Van Der Waals Schottky Junctions, *Adv. Devices Instrum.*, 2023, **4**, 0022, DOI: 10.34133/adi.0022.
5 B. Ezhilmaran, A. Patra, S. Benny, M. R. Sreelakshmi, V. V. Akshay, S. V. Bhat and C. S. Rout, Recent developments in the photodetector applications of Schottky diodes based on 2D materials, *J. Mater. Chem. C*, 2021, **9**, 6122–6150, DOI: 10.1039/D1TC00949D.
6 Y. Tian, H. Liu, J. Li, B. Liu and F. Liu, Recent Developments of Advanced Broadband Photodetectors Based on 2D Materials, *Nanomaterials*, 2025, **15**, 431, DOI: 10.3390/nano15060431.
7 K. Abbas, P. Ji, N. Ullah, S. Shafique, Z. Zhang, M. F. Ameer, S. Qin and S. Yang, Graphene photodetectors integrated with silicon and perovskite quantum dots, *Microsystems Nanoeng.*, 2024, **10**, 81, DOI: 10.1038/s41378-024-00722-4.
8 X. Ji, C. Lu, Z. Yan, L. Shan, X. Yan, J. Wang, J. Yue, X. Qi, Z. Liu, W. Tang and P. Li, A review of gallium oxide-based power Schottky barrier diodes, *J. Phys. D. Appl. Phys.*, 2022, **55**, 443002, DOI: 10.1088/1361-6463/ac855c.
9 F. Jiang, M. Shi, J. Zhou, Y. Bu, J. Ao and X. S. Chen, Integrated Photonic Structure Enhanced Infrared Photodetectors, *Adv. Photonics Res.*, 2021, **2**, 2000187, DOI: 10.1002/adpr.202000187.
10 Q. Li, J. Meng and Z. Li, Recent progress on Schottky sensors based on two-dimensional transition metal dichalcogenides, *J. Mater. Chem. A*, 2022, **10**, 8107–8128, DOI: 10.1039/D2TA00075J.
11 A. A. Hussaini, Y. Torlak, S. Büyükçelebi, M. H. Çolpan, M. Kus and M. Yıldırım, High-performance polyoxometalate/p-Si photodetector enabling bias-free detection across the visible–NIR spectrum, *J. Mater. Sci. Mater. Electron.*, 2026, **37**, 396, DOI: 10.1007/s10854-026-16772-5.
12 J. Zhang, J. Zhang and H. Wei, Perovskite photodetectors on skin: current advances and commercialization challenges, *Sci. China Mater.*, 2025, **68**, 4364–4370, DOI: 10.1007/s40843-025-3570-4.
13 D. Nodari, Z. Qiao, F. Furlan, O. J. Sandberg, K. Vandewal and N. Gasparini, Towards high and reliable specific detectivity in visible and infrared perovskite and organic photodiodes, *Nat. Rev. Mater.*, 2025, **10**, 842–856, DOI: 10.1038/s41578-025-00830-1.
14 J. Ahn, E. Yeon and D. K. Hwang, Recent Progress in 2D Heterostructures for High-Performance Photodetectors and Their Applications, *Adv. Opt. Mater.*, 2025, **13**, 2403412, DOI: 10.1002/adom.202403412.
15 D. Shakthivel, A. S. Dahiya and R. Dahiya, Inorganic semiconducting nanostructures-based printed photodetectors, *Appl. Phys. Rev.*, 2025, **12**(1), 011325, DOI: 10.1063/5.0236154.
16 T. A. Manfo, D. E. Yıldız, A. A. Hussaini, M. Yıldırım and B. Gündüz, The light detection performance of the Al/DCJTB/n-Si Schottky type photodetector for a wide-range spectrum, *Opt. Mater.*, 2026, **169**, 117688, DOI: 10.1016/j.optmat.2025.117688.
17 C. Zhang, W.-T. Shiu, L.-Y. Chang, K. Chu, P. Hu, J. Adsetts, L. Liu, Q. Zhang and Z. Ding, A comparative study of band structures and quantum confinement effects in graphene and nitrogen-doped carbon quantum dots, *Can. J. Chem.*, 2025, **103**, 617–624, DOI: 10.1139/cjc-2024-0241.
18 S. Kumar Thiyagarajan, S. Raghupathy, D. Palanivel, K. Raji and P. Ramamurthy, Fluorescent carbon nano dots from

lignite: unveiling the impeccable evidence for quantum confinement, *Phys. Chem. Chem. Phys.*, 2016, **18**, 12065–12073, DOI: 10.1039/C6CP00867D.

19 L. Thyda, J. K. Joseph, N. Koppula, S. Sana and T. Kuppusamy, Carbon Quantum Dots/ZnO Hybrid Nanostructured Thin Films and UV Photodetector Performances, *Phys. Status Solidi*, 2025, **222**, 2500458, DOI: 10.1002/pssa.202500458.

20 S. Dua, P. Kumar, B. Pani, A. Kaur, M. Khanna and G. Bhatt, Stability of carbon quantum dots: a critical review, *RSC Adv.*, 2023, **13**, 13845–13861, DOI: 10.1039/D2RA07180K.

21 N. Andleeb, S. Zafar, Z. Rahim, M. M. Iqbal, R. Lal and M. A. Farooq, Carbon quantum dots as versatile nanomaterials for improving soil health and plant stress tolerance: a comprehensive review, *Planta*, 2025, **262**, 44, DOI: 10.1007/s00425-025-04758-2.

22 N. A. Pechnikova, K. Domvri, K. Porpodis, M. S. Istomina, A. V. Iaremenko and A. V. Yaremenko, Carbon Quantum Dots in Biomedical Applications: Advances, Challenges, and Future Prospects, *Aggregate*, 2025, **6**, e707, DOI: 10.1002/agt2.707.

23 A. Farid, L. Qiu, X. Zhang, B. Hu, Z. Wu and G. Wang, One-Pot Synthesis of Luminescent Ag–Cu–Ga–S/ZnS Quantum Dots Bridging the Cyan Gap for Ultrahigh-Color-Rendering White-Light-Emitting Diodes, *ACS Appl. Nano Mater.*, 2025, **8**, 14703–14712, DOI: 10.1021/acsanm.5c02386.

24 A. Azam, M. P. Suryawanshi, Y. Liu, J. Shi, Y. Xia, H. Zhang, S. Wang, D. Zhao and S. Li, Quantum Dots-Enabled Downshifting and Downconversion Strategies for Enhanced Photovoltaics, *ACS Nano*, 2025, **19**, 28969–28991, DOI: 10.1021/acsnano.5c04988.

25 P. Xia, B. Sun, M. Biondi, J. Xu, O. Atan, M. Imran, Y. Hassan, Y. Liu, J. M. Pina, A. M. Najarian, L. Grater, K. Bertens, L. K. Sagar, H. Anwar, M. Choi, Y. Zhang, M. Hasham, F. P. García de Arquer, S. Hoogland, M. W. B. Wilson and E. H. Sargent, Sequential Co-Passivation in InAs Colloidal Quantum Dot Solids Enables Efficient Near-Infrared Photodetectors, *Adv. Mater.*, 2023, **35**, 2301842, DOI: 10.1002/adma.202301842.

26 X. Huang, R. Bao and J. Yi, Improving effect of carbonized quantum dots (CQDs) in pure copper matrix composites, *J. Cent. South Univ.*, 2021, **28**, 1255–1265, DOI: 10.1007/s11771-021-4693-y.

27 V. L. John, Y. Nair and T. P. Vinod, Doping and Surface Modification of Carbon Quantum Dots for Enhanced Functionalities and Related Applications, *Part. Part. Syst. Charact.*, 2021, **38**, 2100170, DOI: 10.1002/ppsc.202100170.

28 G. Kandasamy, Recent Advancements in Doped/Co-Doped Carbon Quantum Dots for Multi-Potential Applications, *C*, 2019, **5**, 24, DOI: 10.3390/c5020024.

29 L. Lin, Y. Luo, P. Tsai, J. Wang and X. Chen, Metal ions doped carbon quantum dots: Synthesis, physicochemical properties, and their applications, *TrAC, Trends Anal. Chem.*, 2018, **103**, 87–101, DOI: 10.1016/j.trac.2018.03.015.

30 F. Mustafa, S. Aslam, M. A. Ahmad and J. Ali, Temperature-dependent photoluminescence of heteroatom-doped edge tuned amino-functionalized GQDs nanoshells conjugated with ZnSe QDs, *J. Mater. Sci. Mater. Electron.*, 2025, **36**, 1942, DOI: 10.1007/s10854-025-16022-0.

31 Ç. Kırbıyık Kurukavak, T. Yılmaz, A. Büyükbekar, M. Tok and M. Kuş, Phosphorus doped carbon dots additive improves the performance of perovskite solar cells via defect passivation in MAPbI3 films, *Mater. Today Commun.*, 2023, **35**, 105668, DOI: 10.1016/j.mtcomm.2023.105668.

32 D. G. Babar and S. S. Garje, Nitrogen and Phosphorus Co-Doped Carbon Dots for Selective Detection of Nitro Explosives, *ACS Omega*, 2020, **5**, 2710–2717, DOI: 10.1021/acsomega.9b03234.

33 S. Chandra, D. Laha, A. Pramanik, A. Ray Chowdhuri, P. Karmakar and S. K. Sahu, Synthesis of highly fluorescent nitrogen and phosphorus doped carbon dots for the detection of Fe 3+ ions in cancer cells, *Luminescence*, 2016, **31**, 81–87, DOI: 10.1002/bio.2927.

34 A. F. Shaikh, M. S. Tamboli, R. H. Patil, A. Bhan, J. D. Ambekar and B. B. Kale, Bioinspired Carbon Quantum Dots: An Antibiofilm Agents, *J. Nanosci. Nanotechnol.*, 2019, **19**, 2339–2345, DOI: 10.1166/jnn.2019.16537.

35 G. Kalaiyarasan, J. Joseph and P. Kumar, Phosphorus-Doped Carbon Quantum Dots as Fluorometric Probes for Iron Detection, *ACS Omega*, 2020, **5**, 22278–22288, DOI: 10.1021/acsomega.0c02627.

36 C. Venkateswara Raju, G. Kalaiyarasan, S. Paramasivam, J. Joseph and S. Senthil Kumar, Phosphorous doped carbon quantum dots as an efficient solid state electrochemiluminescence platform for highly sensitive turn-on detection of Cu2+ ions, *Electrochim. Acta*, 2020, **331**, 135391, DOI: 10.1016/j.electacta.2019.135391.

37 X.-D. Mai, Y. T. H. Phan and V.-Q. Nguyen, Excitation-Independent Emission of Carbon Quantum Dot Solids, *Adv. Mater. Sci. Eng.*, 2020, 2020, DOI: 10.1155/2020/9643168.

38 T. K. Mondal, U. K. Ghorai and S. K. Saha, Dual-Emissive Carbon Quantum Dot-Tb Nanocomposite as a Fluorescent Indicator for a Highly Selective Visual Detection of Hg(II) in Water, *ACS Omega*, 2018, **3**, 11439–11446, DOI: 10.1021/acsomega.8b01159.

39 J. Wei, H. Li, Y. Yuan, C. Sun, D. Hao, G. Zheng and R. Wang, A sensitive fluorescent sensor for the detection of trace water in organic solvents based on carbon quantum dots with yellow fluorescence, *RSC Adv.*, 2018, **8**, 37028–37034, DOI: 10.1039/C8RA06732E.

40 Ç. Kırbıyık Kurukavak, A. Büyükbekar, M. Tok, T. Yılmaz, M. Kuş and M. Ersöz, Modification and performance enhancement of P3HT:PCBM based organic solar cells incorporated with phosphorus doped carbon quantum dots, *Chem. Phys. Lett.*, 2024, **845**, 141300, DOI: 10.1016/j.cplett.2024.141300.

41 U. R. R. P. Remli and A. A. Aziz, Photocatalytic degradation of methyl orange using Carbon Quantum Dots (CQDs) derived from watermelon rinds, *IOP Conf. Ser. Mater. Sci. Eng.*, 2020, **736**, 042038, DOI: 10.1088/1757-899X/736/4/042038.

42 A. Gharaati and S. Behaein, Bandgap-engineered carbon quantum dots: eco-friendly synthesis from citrus aurantium

juice and enhanced photocatalytic degradation of malachite green, *Mater. Technol.*, 2025, **40**(1), 2587210, DOI: 10.1080/10667857.2025.2587210.

43 L. Shi, K. Chen, A. Zhai, G. Li, M. Fan, Y. Hao, F. Zhu, H. Zhang and Y. Cui, Status and Outlook of Metal–Inorganic Semiconductor–Metal Photodetectors, *Laser Photon. Rev.*, 2021, **15**(1), 2000401, DOI: 10.1002/lpor.202000401.

44 M. Yilmaz, M. Yaman, F. Yildirim, S. Nuhzat and S. Aydogan, A self-powered and cost-effective rGO/n-Si photodetector with broad spectral response including visible, UV, and near-IR regions, *Mater. Sci. Eng. B*, 2025, **322**, 118659, DOI: 10.1016/j.mseb.2025.118659.

45 J. R. Nicholls, Electron trapping effects in SiC Schottky diodes: Review and comment, *Microelectron. Reliab.*, 2021, **127**, 114386, DOI: 10.1016/j.microrel.2021.114386.

46 F. Gaspari, 2.10 Semiconductors, in *Compare Energy System*, Elsevier, 2018, pp. 266–302, DOI: 10.1016/B978-0-12-809597-3.00221-2.

47 S. Akin and S. Sönmezoğlu, Impact of Copper-Doped Titanium Dioxide Interfacial Layers on the Interface-State and Electrical Properties of Si-based MOS Devices, *Metall. Mater. Trans. A*, 2015, **46**, 4150–4159, DOI: 10.1007/s11661-015-3040-z.

48 H. Kacus, M. Yilmaz, U. Incekara, A. Kocyigit and S. Aydogan, The photosensitive activity of organic/inorganic hybrid devices based on Aniline Blue dye: Au nanoparticles (AB@Au NPs), *Sens. Actuators, A*, 2021, **330**, 112856, DOI: 10.1016/j.sna.2021.112856.

49 Ş. Karataş and N. Berk, Performance of the illumination dependent electrical and photodiode characteristic of the Al/(GO:PTCDA)/p-Si structures, *Opt. Mater.*, 2022, **126**, 112231, DOI: 10.1016/j.optmat.2022.112231.

50 M. H. Çolpan, Performance Analysis of Graphene Oxide Based Photodetector for Broad Spectrum Light Sensing, *Gazi Univ. J. Sci. Part A Eng. Innov.*, 2025, **12**, 1078–1087, DOI: 10.54287/gujsa.1799121.

51 M. H. Çolpan, UV-Vis-NIR Photodetector Produced Using Lavandula angustifolia Extract: A Green Approach, *Int. J. Adv. Nat. Sci. Eng. Res.*, 2025, **9**, 270–276.

52 G. Zhang, S. Zhang, L. Zheng, H. Wu, B. Wang, Z. He, Z. Jin, C. Ye and G. Wang, Localized Surface Plasmon Resonance Enables Si-Based Near-Infrared Photodetector, *IEEE Trans. Electron Devices*, 2023, **70**, 5497–5500, DOI: 10.1109/TED.2023.3303148.

53 M. A. Nazirzadeh, F. B. Atar, B. B. Turgut and A. K. Okyay, Random sized plasmonic nanoantennas on Silicon for low-cost broad-band near-infrared photodetection, *Sci. Rep.*, 2014, **4**, 7103, DOI: 10.1038/srep07103.

54 W. Zhou, L. Zheng, Z. Ning, X. Cheng, F. Wang, K. Xu, R. Xu, Z. Liu, M. Luo, W. Hu, H. Guo, W. Zhou and Y. Yu, Silicon: quantum dot photovoltage triodes, *Nat. Commun.*, 2021, **12**, 6696, DOI: 10.1038/s41467-021-27050-9.

55 S.-W. Lee, K.-J. Choi, B.-H. Kang, J.-S. Lee, S.-W. Kim, J.-B. Kwon, S.-A. Gopalan, J.-H. Bae, E.-S. Kim, D.-H. Kwon and S.-W. Kang, Low dark current and improved detectivity of hybrid ultraviolet photodetector based on carbon-quantum-dots/zinc-oxide-nanorod composites, *Org. Electron.*, 2016, **39**, 250–257, DOI: 10.1016/j.orgel.2016.10.003.

56 L. Thyda, J. K. Joseph, K. Naresh, G. Dasi, S. Suneetha, R. Thangavel, V. Jayalakshmi, P. Amaladass and K. Thangaraju, Green synthesis of carbon quantum dots derived from mango-leaves (M−CQDs): M−CQDs/ZnO nanorods heterostructure thin films for efficient self-powered UV photodetector applications, *Appl. Surf. Sci.*, 2025, **685**, 162032, DOI: 10.1016/j.apsusc.2024.162032.

57 Z. Luo, C. Wu, M. Yan, X. Yu, X. Yu, Q. Qian, Y. Zhou, H. Zhang, Z. Li and G. Long, Enhancing detectivity of organic photodetectors through the biomass carbon quantum dots from sugarcane bagasse, *Mater. Chem. Phys.*, 2024, **316**, 129056, DOI: 10.1016/j.matchemphys.2024.129056.

58 P.-H. Hsiao, Y.-C. Lai and C.-Y. Chen, Dual-sized carbon quantum dots enabling outstanding silicon-based photodetectors, *Appl. Surf. Sci.*, 2021, **542**, 148705, DOI: 10.1016/j.apsusc.2020.148705.

59 Y. Tan, Q. Qiao, T. Weng, Y. Jia, R. Wang, X. Yu, Y. Su, Z. Li and X. Yu, Self-powered photodetector based on poly(3-hexylthiophene)/Zinc oxide quantum dots Organic-inorganic hybrid heterojunction, *Chem. Phys. Lett.*, 2022, **806**, 140033, DOI: 10.1016/j.cplett.2022.140033.